Available online at www.sciencedirect.com
ScienceDirect
Ceramics International 37 (2011) 1259–1264
CERAMICS INTERNATIONAL
www.elsevier.com/locate/ceramint

Structural characterization of barium titanate–cobalt ferrite composite powders

L.V. Leonel [a,b,*], A. Righi [c], W.N. Mussel [d], J.B. Silva [a,b], N.D.S. Mohallem [b]

[a] Comissão Nacional de Energia Nuclear, CDTN/CNEN, Belo Horizonte, MG, Brazil
[b] Laboratório de Materiais Nanoestruturados, DQ, Universidade Federal de Minas Gerais, Belo Horizonte, MG, Brazil
[c] Departamento de Física, ICEx, Universidade Federal de Minas Gerais, Belo Horizonte, MG, Brazil
[d] Laboratório de Raios X, DQ, Universidade Federal de Minas Gerais, Belo Horizonte, MG, Brazil

Received 23 June 2010; received in revised form 28 July 2010; accepted 2 December 2010
Available online 22 February 2011

Abstract

Barium titanate–cobalt ferrite composite powders prepared by sol–gel method and by mixing of precursors were characterized by Raman spectroscopy, scanning electron microscopy and Rietveld refinement of XRD data. Ba vacancies and $BaTiO_3$–$CoFe_2O_4$ interfacial stress were associated to lowering of tetragonal distortion in the ferroelectric structure. Raman spectroscopy suggested the encapsulation of ferrite inside clusters of particles in the sol–gel composite.

Keywords: A. Sol–gel process; Barium titanate; Composite; Ferroelectricity

1. Introduction

Magnetoelectric (ME) materials are promising candidates for technological applications since the multiferroic coupling allows the interconnection between magnetic and electric fields. New memory devices electrically written and magnetically read have been proposed based on ME materials [1].

ME structures can be prepared as single-phase materials or composites combining magnetostrictive and piezoelectric components. In the past few years, ME composites have been subject of many investigations [2–5] since they can yield a giant ME response at room temperature while the single-phase materials exhibit weak magneto-electric coupling at low temperature. The ME coupling in the composite materials depends strongly on their microstructure. Many inherent preparation problems as atomic diffusion and undesirable chemical reactions between phases [6] can affect the interface, modifying its chemical and structural properties and thus lowering the coupling.

$BaTiO_3$–$CoFe_2O_4$ composites are interesting magnetoelectric materials due to the individual properties of their components. $CoFe_2O_4$ has a spinel structure with large coercivity and magnetostriction [7]. $BaTiO_3$ exhibits polymorphs depending on the temperature. The tetragonal polymorph (t-$BaTiO_3$) is the most interesting due to its ferroelectric and piezoelectric properties. The cubic polymorph (c-$BaTiO_3$) is paraelectric. Although the tetragonal-to-cubic transition occurs at the Curie temperature ($T_c \approx 130\ ^\circ C$ in single-crystal), it is well known that c-$BaTiO_3$ can be found at room temperature in very fine particles, below the critical size of 10–35 nm [8–12]. Studies on $BaTiO_3$ ferroelectric behavior relate the cubic structure of ultrafine particles to the lack of long-range cooperative interactions, the presence of internal strains, depolarization fields and structural defects [13,14].

X-ray diffraction (XRD) is a limited method to distinguish between c- and t-$BaTiO_3$ in ultrafine particles due to the extensive broadening of Bragg reflexions. Raman vibrational spectroscopy can provide information on local lattice disorder, defects and has proved to be more sensitive to detect small distortions of the tetragonal unit cell than XRD.

* Corresponding author at: CDTN/CNEN, Av. Antônio Carlos 6627, Cidade Universitária-UFMG, Pampulha, Belo Horizonte 31270-90, MG, Brazil. Tel.: +55 31 30693389.
E-mail address: lvl@cdtn.br (L.V. Leonel).

0272-8842/$36.00
doi:10.1016/j.ceramint.2011.01.017

This work aimed at evaluating the structural properties of $BaTiO_3$ and $CoFe_2O_4$ in single-phase and in composite powders prepared by sol–gel process focusing mainly on the tetragonal distortion of $BaTiO_3$.

2. Synthesis

The syntheses of $BaTiO_3$, $CoFe_2O_4$ and $BaTiO_3$–$CoFe_2O_4$ composite powders were described elsewhere [15]. Briefly, $BaTiO_3$ powder was prepared by sol–gel method and calcined at 900 °C (sample B9) and 1100 °C (sample B11). $CoFe_2O_4$ powder was prepared by coprecipitation followed by freeze-drying and calcination at 900 °C (sample F9) and 1100 °C (sample F11). The composites $BaTiO_3$–$CoFe_2O_4$ 14:11 wt% were prepared by: (a) mixing and calcination of precursor powders of $BaTiO_3$ and $CoFe_2O_4$ at 900 °C (sample M9) and 1100 °C (sample M11); (b) dispersing the $CoFe_2O_4$ precursor powder into $BaTiO_3$ wet gel, drying of the resulting brown gel and calcination of the dried gel at 900 °C (sample C9) and 1100 °C (sample C11).

3. Characterization

Raman spectra were collected using a T64000 Horiba–Jobin Yvon triple–monochromator spectrometer equipped with a confocal microscope and a liquid N_2 cooled charge coupled device (CCD). The scattering was excited using an argon ion laser at 514.5 nm. The spot size of the laser was 1 μm^2 using a 100× objective and the laser power was kept at 1.0 mW in order to avoid sample heating.

XRD data were recorded using a Siemens D5000 diffractometer with Cu Kα radiation and graphite monochromator, 2θ step of 0.05°. The samples were measured under spinning at 60 rpm to prevent preferred orientation. The major crystalline phases were assigned to spinel $CoFe_2O_4$ (JCPDS-22-1086, 1997), c-$BaTiO_3$ (JCPDS-01-0104, 1997) or t-$BaTiO_3$ (JCPDS-05-0626); $BaFe_{12}O_{19}$ (JCPDS-34-0129, 1997) was identified as minor crystalline phase.

Rietveld refinement with FullProf program was performed to evaluate particle size, lattice parameters and microstrain. Due to the low solubility of Ba in comparison with Ti, the stoichiometric Ba/Ti ratio was also evaluated. The Thompson–Cox–Hastings pseudo-Voight function with axial divergence asymmetry was chosen as profile function. The statistics R_{exp}, R_{wp} and GOF were used to evaluate fitness [16].

Scanning electron microscopy (SEM) was carried out using a secondary electron detector (FEI, Quanta 200 FEG). The particulate material was previously dispersed in isopropanol and deposited on a Si plate.

4. Results and discussion

4.1. Raman spectroscopy

The Raman spectra of samples B9, B11, shown in Fig. 1a, were characteristic of t-$BaTiO_3$ as evidenced by the vibrational modes at around 257, 306, 520, 720 cm^{-1} (Table 1). Both

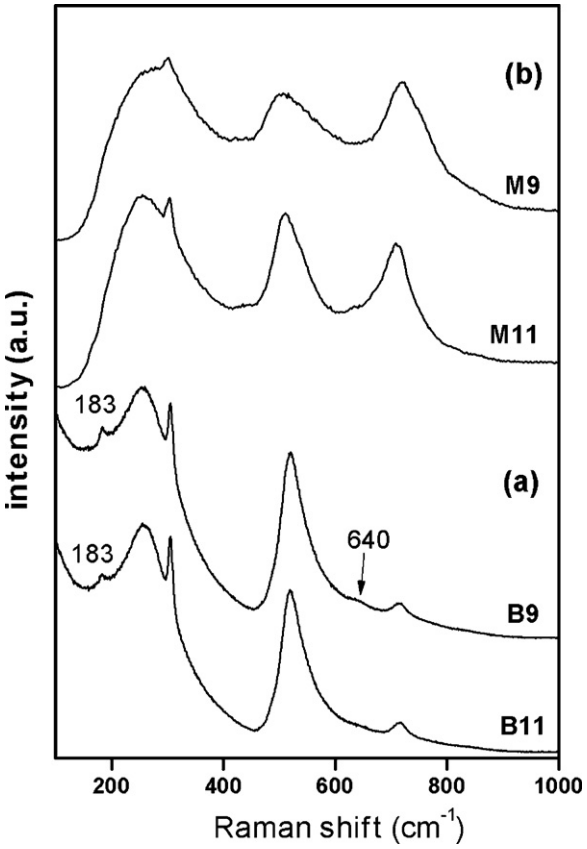

Fig. 1. Raman spectra of samples (a) B9, B11 and (b) M9, M11 (white region).

spectra exhibited a small peak at 183 cm^{-1} that could be ascribed to lattice defects or small amounts of orthorhombic phase [17,18]. Sample B9 showed an interesting feature at 640 cm^{-1} which might be assigned to hexagonal $BaTiO_3$ [19,20]. As this feature decreased with increasing thermal treatment temperature, it was considered to be a satellite peak due to planar defects in the tetragonal structure [21].

In the mixture samples M9, M11, the laser beam could clearly discriminate between white and dark regions assigned to t-$BaTiO_3$ and $CoFe_2O_4$ particles, respectively. Typical Raman spectra of white regions, shown in Fig. 1b, presented t-$BaTiO_3$ characteristic modes. The bands were broader than those found in samples B9, B11, suggesting decreased structural coherence [11]. The higher intensity of the band at ≈720 cm^{-1} relative to the band at ≈510 cm^{-1} was also found by Busca et al. [22] and assigned to particles with sub-stoichiometric Ba/Ti ratio due to Ba segregation as $BaCO_3$. $BaTiO_3$ vibrational modes were downshifted in comparison with the corresponding modes in samples B9, B11, as shown in Table 1.

Table 1
Raman vibrational modes in $BaTiO_3$ samples and white region of the composite samples (M).

Sample	Raman shift (cm^{-1})			
B9, B11	256, 259	305, 306	521, 519	718, 722
M9, M11	274, 255	301, 304	506, 510	722, 711
$BaTiO_3$[a]	242, 266	303, 311	514, 530	713, 720

[a] Polycrystalline as reported in Refs. [9,11,12,17,18,21,32–34].

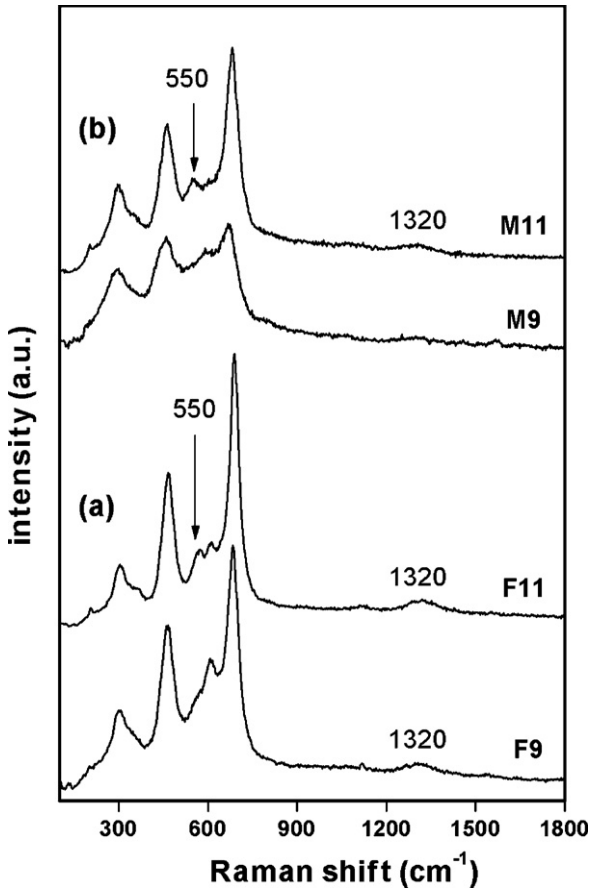

Fig. 2. Raman spectra of samples (a) F9, F11 and (b) M9, M11 (dark region).

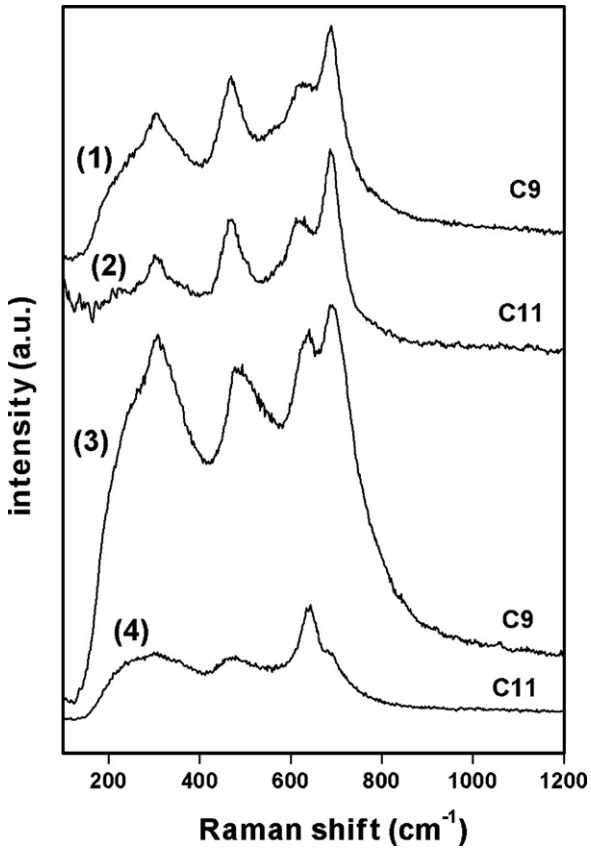

Fig. 3. Raman spectra of different regions of samples C9, C11.

Fig. 2a shows the spectra of samples F9, F11. The vibrational modes were close to those reported for polycrystalline $CoFe_2O_4$, as shown in Table 2. The broad band centered at ≈1320 cm^{-1} can be assigned to hematite [23]. The appearing of the mode at about 550 cm^{-1} was attributed to a decrease of symmetry in the octahedral site due to ferrihydrite formation [24].

The spectra of dark regions of samples M9, M11, shown in Fig. 2b, were close to those of samples F9, F11, with broader bands attributed to lower crystallinity and/or smaller particle size. However, the vibrational modes related to octahedral (≈680 cm^{-1}) and tetrahedral (≈470 cm^{-1}) spinel sublattices [25] were clearly shifted in comparison with those of pure $CoFe_2O_4$ samples (Table 2). The upshift in $CoFe_2O_4$ vibrational modes as well as the downshift in $BaTiO_3$ vibrational modes may be due to the existence of $BaTiO_3$–$CoFe_2O_4$ interfacial stress causing lattice strain.

Table 2
Raman vibrational modes in $CoFe_2O_4$ samples, dark region of the composite samples (M) and different regions of the composite samples (C).

Sample/spectra	Raman shift (cm^{-1})				
F9, F11	216, 203	281, 298	457, 461	591, 610	672, 682
M9, M11	201, 206	299, 303	463, 466	607, 610	684, 689
C9/1	203	300	467	[b]	688
C11/2	214	299	466	[b]	688
C9/3	200	305	484	[b]	696
C11/4	207	295	468	[b]	691
$CoFe_2O_4$[a]	190–203	289–330	451–470	595–650	663–690

[a] Polycrystalline as reported in Refs. [24,31,35].
[b] Peak not observed.

It was difficult to distinguish between dark and white regions in samples C9, C11 due to the good dispersion of $CoFe_2O_4$ and $BaTiO_3$ particles in the area scanned by the laser beam (1 μm^2). This suggests that samples C9, C11 present higher interfacial area than samples M9, M11. Two typical spectra for each sample are identified in Fig. 3. Except for the peak at about 600 cm^{-1}, the broad vibrational modes due to $CoFe_2O_4$ were observed, as shown in Table 2. The vibrational modes due to t-$BaTiO_3$ were not observed. The peak at around 640 cm^{-1} was attributed to small amounts of hexagonal $BaTiO_3$ also identified by XRD (see Section 4.2). Although c-$BaTiO_3$ is expected to be inactive, two broad bands at around 250 and 520 cm^{-1} due to Ti^{4+} disorder in the cubic structure have been reported [17]. Therefore, both spectra were fitted with the broad features of c-$BaTiO_3$.

In spectra (1) and (2), shown in Fig. 3, the vibrational modes due to $CoFe_2O_4$ octahedral and tetrahedral sublattices (Table 2) were close to those of samples M9, M11. However, these modes were strongly upshifted in spectra (3) and slightly upshifted in spectra (4). The strong blueshift may be result of the presence of some $CoFe_2O_4$ particles encapsulated inside clusters of $BaTiO_3$ particles in sample C9. This structure must have been destroyed upon thermally treating the composite sample at higher temperature, turning down the $CoFe_2O_4$ vibrational modes in sample C11. Raman shift has already been observed

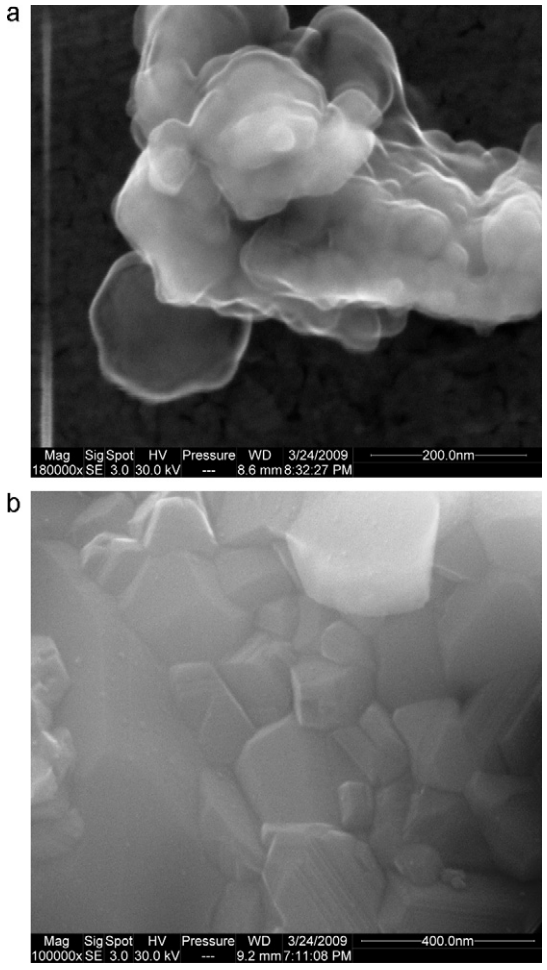

Fig. 4. SEM micrograph of samples (a) C9 and (b) C11.

by other authors in encapsulated structures and assigned to the existence of a stressed core/tensile shell configuration resulting from differences in the corresponding lattice constants [26,27]. The shift values were used to estimate shell thickness [28].

The encapsulated structure was also suggested by SEM analysis. Fig. 4 shows SEM images of samples C9 and C11. The SEM micrograph of sample C9 (Fig. 4a) suggests the existence of clusters of particles which were not observed in sample C11 (Fig. 4b) due probably to the diffusion between the phases at high temperature.

4.2. Rietveld refinement

The Rietveld refinement was carried out according to Raman spectroscopy results, which indicated the presence of t-$BaTiO_3$ in samples B9, B11, M9, M11 and c-$BaTiO_3$ in samples C9, C11 as major $BaTiO_3$ crystalline phase. Fig. 5 shows the theoretical and experimental diffraction patterns of single-phase and composite samples calcined at 1100 °C. The difference between theoretical and experimental patterns is also shown. The $CoFe_2O_4$ and $BaTiO_3$ structural parameters obtained by refinement as well as the corresponding uncertainties (into brackets) given by FullProf program are shown in Tables 3 and 4. In order to help the discussion on the

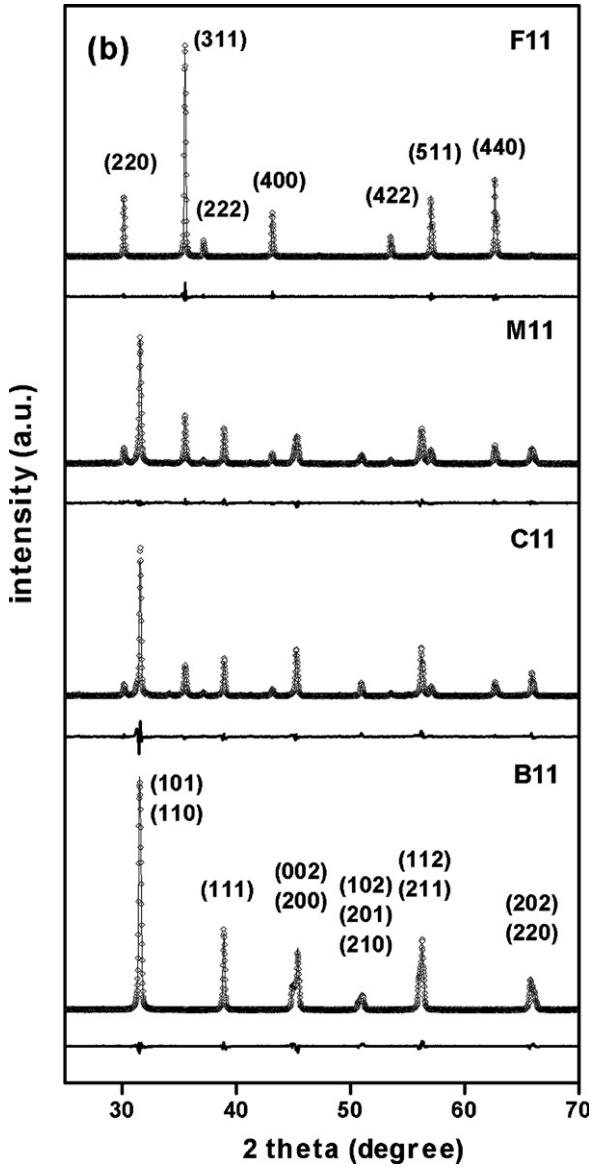

Fig. 5. Experimental (line) and theoretical (symbol) diffraction patterns of $CoFe_2O_4$, $BaTiO_3$ and composite samples calcined at 1100 °C.

$BaTiO_3$ tetragonal distortion, the structural parameters in Table 4 were presented in descending order of *c*/*a* ratio.

The theoretical diffraction pattern of sample B11, supposing the tetragonal polymorph as the only $BaTiO_3$ crystalline phase, did not match well with the experimental pattern (R_{exp} = 8.97%, R_{wp} = 15.40%, GOF = 1.72). This lack of agreement can be ascribed to a broad particle size distribution [29,30]. To attain

Table 3
Structural parameters of $CoFe_2O_4$ in single-phase and composite samples.

Sample	Crystallite size (nm)	*a* (Å)	$\varepsilon \times 10^4$
F11	316(30)	8.3830(2)	8.9(0.9)
F9	174(14)	8.3858(3)	9.1(0.9)
M11	109(13)	8.3841(1)	10(1)
M9	78(8)	8.3822(4)	10(2)
C11	86(5)	8.3814(4)	18(1)
C9	21(3)	8.3717(5)	19(2)

Table 4
Structural parameters of $BaTiO_3$ in single-phase and composite samples.

Sample	*c/a*	Ba/Ti	$\varepsilon \times 10^4$	Crystallite size (nm)	*a* (Å)	*c* (Å)
B11[a]	1.010	0.94	9.2(0.5)	138(12)	3.9940(6)	4.0341(9)
M11[a]	1.009	0.94	4.2(0.8)	[b]	3.9943(4)	4.0295(6)
B9	1.006	0.93	18(2)	57(7)	4.0004(8)	4.0230(4)
B11[a]	1.004	0.89	20(3)	318(100)	4.0046(3)	4.0199(4)
M11[a]	1.004	0.92	18(2)	98(18)	4.0024(6)	4.0165(3)
M9	1.003	0.89	79(9)	73(9)	4.0043(9)	4.0176(8)
M9		0.89	10(5)	27(4)	4.0234(8)	
C9		0.90	28(3)	59(3)	4.0136(9)	
C11		0.92	22(3)	169(27)	4.0060(8)	

[a] Sample with bimodal particle size distribution.
[b] Crystallite size not reported due to high uncertainty.

better fit, we proposed a bimodal t-$BaTiO_3$ particle size distribution which resulted in smaller residues (R_{exp} = 9.01%, R_{wp} = 12.40%, GOF = 1.38). Both fits, in the range 44.4–46.0° 2θ, are shown in Fig. 6a (unimodal) and Fig. 6b (bimodal particle size distribution). The diffraction pattern of sample M11 was also fitted using a bimodal particle size distribution model (R_{exp} = 11.41%, R_{wp} = 16.10%, GOF = 1.41).

Regarding composite sample C9, the large overlapping of reflexions due to $CoFe_2O_4$, $BaTiO_3$ and $BaFe_{12}O_{19}$ phases, the third attributed to interfacial reaction, was responsible for the high residues (R_{exp} = 12.6%, R_{wp} = 18.4%, GOF = 1.46). The misfit in the region corresponding to the plane (1 1 0) in the diffraction pattern of sample C11 was due to formation of small amounts of hexagonal $BaTiO_3$ as indicated by an incipient reflexion at 2θ = 26° and by Raman spectroscopy.

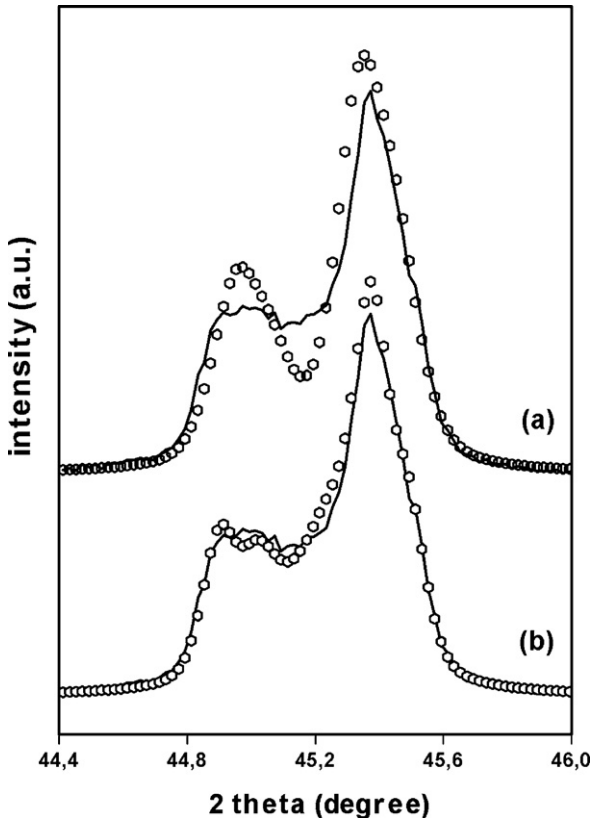

Fig. 6. Experimental (line) and theoretical (symbol) diffraction patterns of sample B11 with (a) unimodal and (b) bimodal particle size distribution.

$CoFeO_4$ crystallite size was lower in composite samples M9, M11, C9, C11 than in pure samples F9, F11. The smaller $CoFe_2O_4$ lattice parameter, a, in the composite samples was attributed to the higher surface tension in small particles as found by QU and co-laborators [31]. The reduction of the lattice parameter in $CoFe_2O_4$ samples, from 8.3858 to 8.3830 Å, was probably due to the densification process [7] at high temperature. $CoFe_2O_4$ particles presented smaller microstrain in samples F9, F11 than in samples C9, C11 probably due to the higher crystallite size and the higher crystallinity suggested by Raman spectroscopy.

Concerning $BaTiO_3$ particles, it is well known that the tetragonal cell asymmetry depends on their size. Smaller distortions are expected to be found for smaller particles [8,13]. The theoretical c/a ratio of bulk $BaTiO_3$ is 1.011. In this work, the tetragonality (c/a) of $BaTiO_3$ particles in samples B9, B11, M9, M11 was more affected by Ba/Ti ratio and microstrain than by particle size (Table 4). Low *c/a* values were accompanied by substoichiometric Ba/Ti ratio and high microstrain. It is well established that the ferroelectric transition is caused by distortion of the oxygen octahedron accompanied by off-center displacement of Ti^{4+}. However, Ba vacancies can create local strain in the lattice, lowering the cooperative displacement of Ti^{4+} and O^{2-} ions. It is worth noting that the smallest *c/a* ratio (1.003) was related to the smallest Ba/Ti stoichiometric ratio and highest microstrain.

In the composite samples C9, C11, the lack of tetragonal transition could not be explained only by strain resulting from Ba vacancies. In this case, it is possible that higher $BaTiO_3$ lattice stress occurred during the thermal treatment of these composite samples due to their higher interfacial area [20]. Particles with substoichiometric Ba/Ti ratio might not have been able to accommodate this additional lattice stress and simultaneously stabilize the tetragonal lattice vibrations thus preventing phase transition.

5. Conclusion

The tetragonality of polycrystalline $BaTiO_3$ prepared by sol–gel method was severely affected by the presence of Ba vacancies. In $BaTiO_3$–$CoFe_2O_4$ composite samples, Ba

vacancies as well as interfacial stress seem to play a role in lowering the tetragonal distortion. The $BaTiO_3$ cubic polymorph was stabilized at room temperature in the composite with the highest interfacial area even though its particle size was found to be higher than the critical value reported in the literature. These results indicate the destabilization of phonons by lattice defects and stress.

Raman vibrational spectroscopy suggested the encapsulation of ferrite inside clusters of particles. This structure was destroyed upon thermally treating the composite at high temperature.

Acknowledgments

The authors wish to acknowledge the cooperation of Maria Sylvia Silva Dantas (UFMG) and J.B.S. Barbosa (CDTN), the financial support of CNPq and FAPEMIG (Brazilian funding agencies) and the technicians of the Center of Microscopy/ UFMG.

References

[1] J.F. Scott, Multiferroic memories, Nat. Mater. 6 (2007) 256–257.
[2] H. Zheng, J. Wang, S.E. Lofland, Z. Ma, L. Mohaddes-Ardabili, T. Zhao, L. Salamanca-Riba, S.R. Shinde, S.B. Ogale, F. Bai, D. Viehland, Y. Jia, D.G. Schlom, M. Wuttig, A. Roytburd, R. Ramesh, Multiferroic $BaTiO_3$–$CoFe_2O_4$ nanostructures, Science 303 (2004) 661–663.
[3] S.Q. Ren, et al., $BaTiO_3$–$CoFe_2O_4$ particulate composites with large high frequency magnetoelectric response, J. Mater. Sci. 40 (2005) 4375–4378.
[4] L. Weng, Y. Fu, S. Song, J. Tang, J. Li, Synthesis of lead zirconate titanate–cobalt ferrite magnetoelectric particulate composites via an ethylenediaminetetraacetic acid–citrate gel process, Scripta Mater. 56 (2007) 465–468.
[5] V. Corral-Flores, D. Bueno-Baqués, R.F. Ziolo, Synthesis and characterization of novel $CoFe_2O_4$–$BaTiO_3$ multiferroic core–shell-type nanostructures, Acta Mater. 58 (2010) 764–769.
[6] C.W. Nan, M.I. Bichurin, S. Dong, D. Viehland, G. Srinivasan, Multiferroic magnetoelectric composites: historical perspectives, status and future directions, J. Appl. Phys. 103 (2008) 031101.
[7] J.B. Silva, W. Brito, N.D.S. Mohallem, Influence of heat treatment on cobalt ferrite ceramic powders, Mater. Sci. Eng. B 112 (2004) 182–187.
[8] M.H. Frey, D.A. Payne, Grain-size effect on structure and phase transformations for barium titanate, Phys. Rev. B 54–5 (1996) 3158–3168.
[9] S. Wada, H. Chikamori, T. Noma, T. Suzuki, Synthesis of nm-sized barium titanate crystallites using a new LTDS method and their characterization, J. Mater. Sci. 35 (2000) 4857–4863.
[10] Z. Zhao, V. Buscaglia, M. Viviani, M.T. Buscaglia, L. Mitoseriu, A. Testino, M. Nygren, M. Johnsson, P. Nanni, Grain-size effects on the ferroelectric behavior of dense nanocrystalline $BaTiO_3$ ceramics, Phys. Rev. B 70 (2004) 024107.
[11] M.B. Smith, K. Page, T. Siegrist, P. Redmond, E.C. Walter, R. Seshadri, L.E. Brus, M.L. Steigerwald, Crystal structure and the paraelectric-to-ferroelectric phase transition of nanoscale $BaTiO_3$, J. Amer. Cer. Soc. 130 (2008) 6955–6963.
[12] T. Takeuchi, M. Tabuchi, K. Ado, K. Honjo, O. Nakamura, H. Kageyama, Y. Suyama, N. Ohtori, M. Nagasawa, Grain-size dependence of dielectric properties of ultrafine $BaTiO_3$ prepared by a sol–crystal method, J. Mater. Sci. 32 (1997) 4053–4060.
[13] K. Uchino, E. Sadanaga, T. Hirose, Dependence of the crystal structure on particle size in barium titanate, J. Am. Ceram. Soc. 72–8 (1989) 1555–1558.
[14] T. Noma, S. Wada, M. Yano, T. Suzuki, Analysis of lattice vibration in fine particles of barium titanate single crystal including the lattice hydroxyl group, J. Appl. Phys. 80–9 (1996) 5223–5232.
[15] L.V. Leonel, N.D.S. Mohallem, J.B. Silva, Preparation of ferroic materials by sol–gel process, in: XV International Sol–Gel Conference, 2009.
[16] R.A. Young, The Rietveld Method, first ed., Oxford University Press, New York, 2006.
[17] Y. Shiratori, C. Pithan, J. Dornseiffer, R. Waser, Raman scattering on nanocrystalline $BaTiO_3$ Part I-isolated particles and aggregates, J. Raman Spectrosc. 38 (2007) 1288–1299.
[18] C.J. Xiao, C.Q. Jin, X.H. Wang, Crystal structure of dense nanocrystalline $BaTiO_3$ ceramics, Mater. Chem. Phys. 111 (2008) 209–212.
[19] M. Arima, M. Kakiana, Y. Nakamura, M. Yashima, M. Yoshimura, Polymerized complex route to barium titanate powders using barium-titanium mixed-metal citric acid complex, J. Am. Ceram Soc. 79–11 (1996) 2847–2856.
[20] Q. Huang, L. Gao, J. Sun, Effect of adding carbon nanotubes on microstructure, phase tranformation and mechanical property of $BaTiO_3$ ceramics, J. Am. Ceram. Soc. 88–12 (2005) 3515–3518.
[21] W. Cho, Structural evolution and characterization of $BaTiO_3$ nanoparticles synthesized from polymeric precursor, J. Phys. Chem. Solids 59–5 (1998) 659–666.
[22] G. Busca, V. Buscaglia, M. Leoni, P. Nanni, Solid state and surface spectroscopic characterization of $BaTiO_3$ fine powders, Chem. Mater. 6 (1994) 955–961.
[23] D.L.A. Faria, V. Silva, M.T. Oliveira, Raman microspectroscopy of some iron oxides and oxyhydroxides, J. Raman Spectrosc. 28 (1997) 873–878.
[24] S. Ayyapapan, J. Philip, B. Raj, Effect of digestion time on size and magnetic properties of spinel $CoFe_2O_4$ nanoparticles, J. Phys. Chem. C 113 (2009) 590–596.
[25] W.H. Wang, X. Ren, Flux growth of high-quality $CoFe_2O_4$ single crystal and their characterization, J. Cryst. Growth 289 (2006) 605–609.
[26] Y. Zhou, C.Y. Wang, H.J. Liu, Y.R. Zhu, Z.Y. Chen, Preparation and studies of Ag–TiO_2 hybrid nanoparticles of core-shell structure, Mater. Sci. Eng. B 67 (1999) 95–98.
[27] P.K. Mohseni, A.D. Rodrigues, J.C. Galzerani, Y.A. Pusep, R.R. LaPierre, Structural and optical analysis of GaAsP/GaP core-shell nanowires, J. App. Phys. 106 (2009) 124306.
[28] L. Lu, X.L. Xu, W.T. Liang, H.F. Lu, Raman analysis of CdSe/CdS core-shell quantum dots with different shell thickness, J. Phys. Condens. Matter 19–40 (2007) 406221.
[29] H.P. Beck, W. Eiser, R. Haberkorn, Pitfalls in the synthesis of nanoscaled perovskite type compounds. Part I: Influence of different sol–gel preparation methods and characterization of nanoscaled $BaTiO_3$, J. Eur. Ceram. Soc. 21 (2001) 687–693.
[30] M.H. Frey, D.A. Payne, Synthesis and processing of barium titanate ceramics from alkoxide solutions and monolithic gels, Chem Mater. 7 (1995) 123–129.
[31] Y. Qu, H. Yang, N. Yang, Y. Fan, H. Zhu, G. Zou, The effect of reaction temperature on the particle size, structure and magnetic properties of coprecipitated $CoFe_2O_4$ nanoparticles, Mater. Lett. 60 (2006) 3548–3552.
[32] W. Cho, E. Hamada, Synthesis of ultrafine $BaTiO_3$ particles from polymeric precursor: their structure and surface property, J. Alloys Compd. 266 (1998) 118–122.
[33] U. Hwang, H. Park, K. Koo, Low temperature synthesis of fully crystallized $BaTiO_3$ particles by the gel–sol method, J. Am. Ceram. Soc. 87–12 (2004) 2168–2174.
[34] Y.C. Zhang, G.L. Wang, K.W. Li, M. Zhang, X.Y. Hu, H. Wang, Facile synthesis of submicron $BaTiO_3$ crystallites by a liquid–solid reaction method, J. Cryst. Growth 290 (2006) 513–517.
[35] F. Nagakomi, S.W. Silva, V.K. Garg, A.C. Oliveira, P.C. Morais, A. Franco Júnior, E.C.D. Lima, The influence of cobalt population on the structural properties of $Co_xFe_{3-x}O_4$, J. Appl. Phys. 101 (2007) 09M514.